nature communications

Article

https://doi.org/10.1038/s41467-026-70805-5

The *Mycobacterium abscessus* cytochrome *bcc:aa*$_3$ oxidase structure paves the way for an agent targeting subunit QcrB

Received: 22 September 2025

Accepted: 4 March 2026

Published online: 03 April 2026

Check for updates

Vikneswaran Mathiyazakan[1], Emilia Xin Yi Tan[1], Garrett Moraski[2], Sandip Basak[1,3], Wuan-Geok Saw[3], Kevin Pethe[4,5,6,7] & Gerhard Grüber[1]

The cytochrome *bcc:aa*$_3$ oxidase is the target of telacebec, a clinically advanced drug developed for *Mycobacterium tuberculosis*. However, telacebec is inactive against *Mycobacterium abscessus*, an opportunistic pathogen increasingly linked to chronic pulmonary infections and notoriously known for intrinsic resistance to numerous antibiotics. Here, we report the 2.6 Å cryo-electron microscopy structure of the *M. abscessus bcc:aa*$_3$ cytochrome oxidase supercomplex, revealing key pathways and the evolution of the mycobacterial QcrB menaquinol-binding cavity. Structure-guided mutagenesis identified polymorphisms that modulate telacebec binding and potency in both *M. abscessus* and *Mycobacterium smegmatis*. Leveraging these insights, we designed ND-011458, a QcrB inhibitor with potent activity against *M. abscessus* and being bactericidal in combination with Clofazimine. The 2.26 Å inhibitor-bound structure elucidates its binding mode and provides a framework for the design of next-generation inhibitors for *M. abscessus* pulmonary diseases.

Cytochrome *bcc:aa*$_3$ oxidases (cyt-*bcc:aa*$_3$) are central components of the mycobacterial electron transport chain (ETC), catalysing the terminal reduction of oxygen to water and driving oxidative phosphorylation via the F-ATP synthase[1]. As inefficient fermenters, mycobacteria derive most of their ATP from oxidative phosphorylation, rendering the ETC a particularly attractive target space[2]. The *bcc:aa*$_3$ supercomplex merges the functionalities of mitochondrial cytochrome bc_1 (complex III), cytochrome aa_3 (complex IV), and a cytochrome *c*-like module, and shows substantial architectural divergence from human and Gram-negative counterparts[3–5], a property that can be exploited to minimize host toxicity and improve target specificity. Electron transfer is initiated by menaquinol (MQH_2) binding to the QcrB Qo site; the first electron proceeds to the FeS cluster and then through a defined cascade of heme and copper cofactors to the catalytic site where O_2 is reduced to water, while the second electron feeds heme b_L and heme b_H to complete the Q-cycle, regenerating MQH_2[3].

Targeting QcrB has proven effective in *Mycobacterium tuberculosis* (*Mtb*), with the clinical-stage compound telacebec (Q203) displaying high potency[6], efficacy in a human phase 2 clinical trial[7] and activity against other mycobacterial species[8–10]. However, Q203 is inactive against *Mycobacterium abscessus* (*Mab*), a rapidly growing non-tuberculous mycobacterium increasingly associated with pulmonary disease in most countries[11–13], due to naturally occurring QcrB polymorphisms[14]. While the structure of the *Mycobacterium smegmatis*[3,4] and *Mtb bcc:aa*$_3$ cytochrome oxidase[3,15] has been resolved, enabling comparative insights into mycobacterial respiratory complexes, no structure for *Mab* is available. This has precluded atomistic understanding of Q203 inactivity in this species and limited structure-guided design of new inhibitors.

Here, we report the expression, purification, and cryo-electron microscopy structure of a functional *Mab bcc:aa*$_3$ cytochrome oxidase supercomplex at 2.6 Å resolution. Structure-guided mutagenesis

[1]School of Biological Sciences, Nanyang Technological University, Singapore, Republic of Singapore. [2]Montana State University, 103 Chemistry and Biochemistry Building, Bozeman, MT, USA. [3]NTU Institute of Structural Biology, Nanyang Technological University, Singapore, Singapore. [4]Lee Kong Chian School of Medicine, Nanyang Technological University, Singapore, Republic of Singapore. [5]National Centre for Infectious Diseases (NCID), Singapore, Singapore. [6]Singapore Centre on Environmental Life Sciences Engineering (SCELSE), Singapore, Singapore. [7]Ineos Oxford Institute for Antimicrobial Research (IOI), Department of Biology, University of Oxford, Oxford, UK. e-mail: ggrueber@ntu.edu.sg

identified residues that modulates Q203 potency in *Mab*, supporting the QcrB Q_o site as a tractable pocket for structure-guided inhibitor design. Leveraging these insights, we identified ND-011458, a QcrB inhibitor with potent growth inhibitory activity against *Mab*. The 2.3 Å inhibitor-bound structure elucidates its binding mode and provides a framework for rational optimization. Combining ND-011458 with clofazimine (CFZ), a redox-active compound activated by NADH dehydrogenase II[16], enhanced *Mab* growth inhibition and killing activity, opening an avenue for an efficient dual-drug combination.

Results and Discussion

Purification and structure determination of the *Mab* cyt-*bcc*:*aa*$_3$ oxidase

The ORBIT (Oligonucleotide-mediated Recombineering followed by Bxb1 Integrase Targeting) system[17] was adapted in *Mab* for the successful integration of a C-terminal genomic FLAG tag to the QcrB domain of the cyt-*bcc*:*aa*$_3$ oxidase for anti-FLAG purification (Fig. 1A). SDS-PAGE (Fig. 1B) and MALDI analysis (Supplementary Tables 1–5) of the eluted supercomplex confirms the first successful production of a recombinant *Mab* subsp. *abscessus* cyt-*bcc*:*aa*$_3$ oxidase, the presence of subunits QcrA-C, CtaC, CtaD, CtaE, CtaF, CtaI, CtaJ, and the accessory unit LpqE. The stable and intact supercomplex formed a single band at the 873.4 kDa region in native PAGE (Fig. 1C). Heme absorbance spectra analysis revealed the presence of hemes *a, b* and *c*, confirming an uninterrupted electron transfer pathway (Fig. 1D). Oxidase activity of the purified enzyme is preserved in the 2,3-dimethyl-[1,4]naphthohydroquinone (DMNQ) oxidoreductase activity assay where a 40% reduction in oxygen levels was observed (Fig. 1E).

The purified supercomplex was subsequently concentrated and applied to a glow-discharged holey copper grid and analyzed by single-particle cryo-EM (Supplementary Fig. 1A, B). 6,845 movies were collected and subsequently curated with the following thresholds: CTF fit resolution Min: 3.597 Å; Max: 7 Å and Astigmatism Min: 0.47 Å; Max: 500 Å resulting in the acceptance of 5,541 exposures for downstream processing. The accepted exposures yielded 249,718 particles that were refined to reach an overall resolution of 3.2 Å (Supplementary Fig. 1C, D). The employment of 3D classification and further refinements improved the overall resolution to 2.6 Å (Supplementary Fig. 1C, D) and permitted de novo modelling of the supercomplex into a composite map (Supplementary Fig. 1E). The cryo-EM map statistics and model statistics are presented in Supplementary Tables 6, 7).

High-resolution structure of the dimeric *Mab* cyt-*bcc*:*aa*$_3$ supercomplex

The 2.6 Å resolution structure of the *Mab* subsp. *abscessus* cyt-*bcc*:*aa*$_3$ oxidase is characterized by the presence of a C2 symmetrical homodimer formed by the cyt-*bcc* and cyt-*aa*$_3$ domains with a linear dimeric cyt-*aa*$_3$-[cyt-*bcc*]$_2$-cyt-*aa*$_3$ arrangement (Fig. 2A). The dimeric cyt-*bcc* core, which orchestrates the Q-cycle, houses subunits QcrA, QcrB and QcrC. QcrA comprises of three transmembrane helices (TMHs) and a

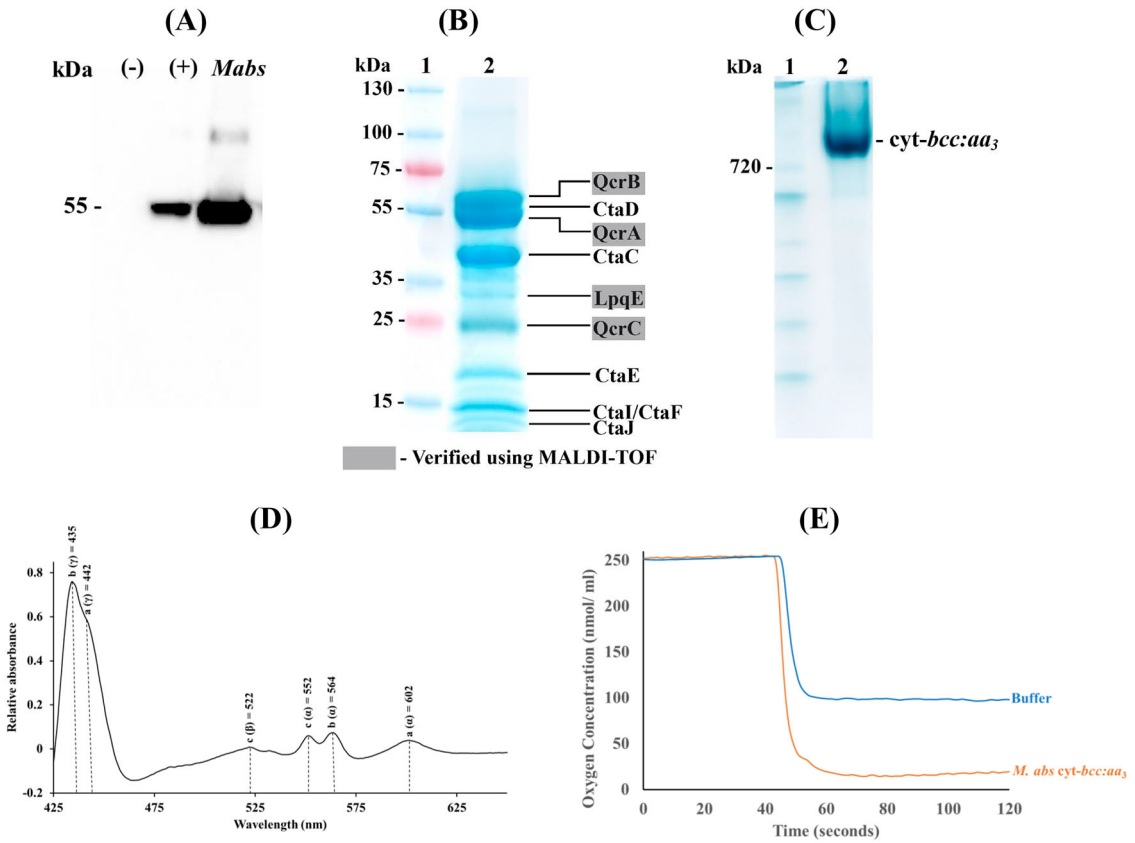

Fig. 1 | Characterization of purified *Mab* subsp. *abscessus* cyt-*bcc*:*aa*$_3$. **A** Western blot analysis confirms expression of QcrB C-terminal genomic FLAG tag in recombinant *Mab* strain derived from ORBIT-promoted gene alteration (Lane 4) with positive (+, *Mtb* cyt-*bcc*:*aa*$_3$ with QcrB C-terminal FLAG tag, Lane 3) and negative (-, *Mab* WT, Lane 2) controls. Data is derived from a single experiment. The experiment was (**B**) 12% SDS gel profile of purified supercomplex. The bands for QcrB, QcrA, QcrC and LpqE were further confirmed through matrix-assisted laser desorption/ionization-time of flight (MALDI-TOF) mass spectrometry (MS) (see Tables 1 to 5 in the supplemental material). Data is a representative from $n = 3$ replicates. **C** Native gel profile indicates a stable homogenous complex via the formation of a single band for the purified *M. abscessus* cyt-*bcc*:*aa*$_3$. Data is derived from a single experiment. **D** Difference spectrum of purified *M. abscessus* cyt-*bcc*:*aa*$_3$ after reduction with $Na_2S_2O_4$. The spectrum registered peaks for heme *a* (442 nm, 602 nm), heme *b* (435 nm, 564 nm), and heme *c* (522 nm, 552 nm). **E** Characterization of the purified enzyme in an oxygen consumption assay. In the presence of 2,3-dimethyl-[1,4]naphthohydroquinone, the purified supercomplex rapidly reduced oxygen levels by approximately 50%, as shown by the profile after subtracting background activity. Source data are provided as a Source Data file.

https://doi.org/10.1038/s41467-026-70805-5

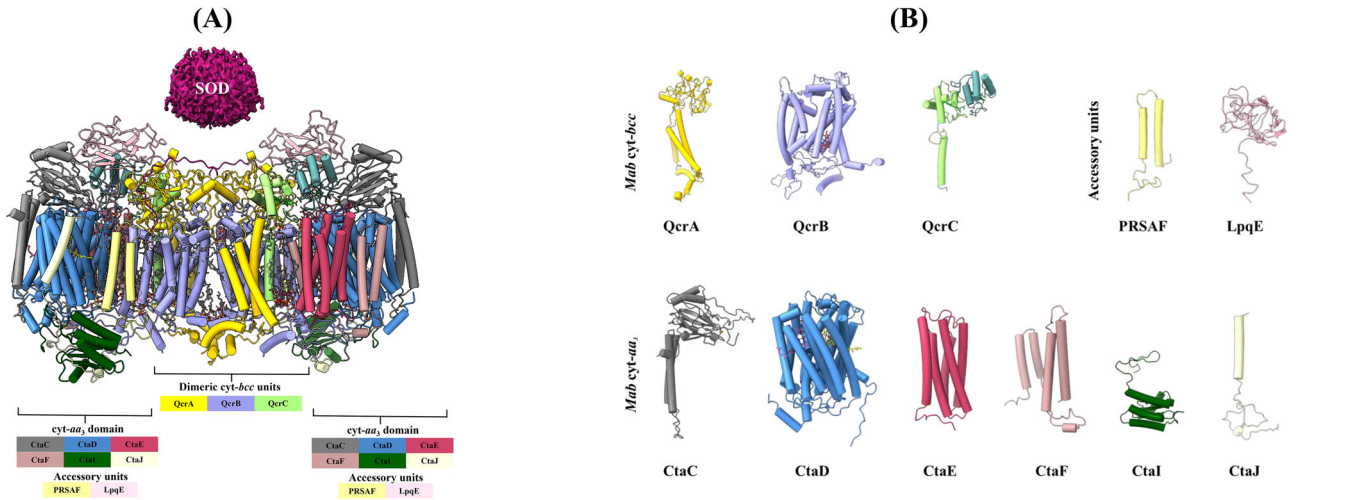

Fig. 2 | Architecture of *M. abscessus* cyt-*bcc*:*aa*$_3$ supercomplex. A Dimeric cryo-EM structure of the resolved *M. abscessus* cyt-*bcc*:*aa*$_3$ oxidase. The cyt-*bcc* subunits in the structure consist of QcrC (green and turquoise), QcrA (yellow), and QcrB (indigo). The cyt-*aa*$_3$ subunits constitute CtaC (gray), CtaD (blue), CtaE (magenta), CtaF (brown), CtaI (forest green) and CtaJ (cream). Accessory units consist of PRSAF (light yellow) and LpqE (light pink). **B** Structural subunits and accessory units of the *M. abscessus* cyt-*bcc*:*aa*$_3$ supercomplex.

periplasmic domain carrying a [2Fe-2S] cluster (Fig. 2B, Supplementary Figs. 2, 3). QcrB comprises of eight TMHs, a low-potential heme b_L within the periplasmic region, and a high-potential heme b_H within the cytoplasmic region (Fig. 2B). QcrC consists of a periplasmatic domain with two heme-containing cytochrome *c* domains, referred to as cyt-c_I and cyt-c_{II}, followed by a single transmembrane-spanning α-helix (Fig. 2B).

The flanking cyt-*aa*$_3$ domains, which belong to the heme-copper oxidase family, catalyse oxygen reduction and are composed of subunits CtaC, CtaD, CtaE, CtaF, CtaI, and CtaJ (Fig. 2A, B, Supplementary Fig. 2). The SC architecture is stabilised by accessory subunits LpqE and PRSAF1 (prokaryotic respiratory supercomplex association factor 1). The unique association of the superoxide dismutase SodC at the periplasmic domain of cyt-*bcc*, proposed to enable detoxification of reactive oxygen species (ROS) generated by cyt-*bcc*, is also seen in *Mab* at 7.5 Å resolution (Fig. 2A). The density of the SodC was cropped from ChimeraX and added separately to the 2.6 Å cryo-EM map to highlight the presence and association of the dismutase to the *Mab* cyt-*bcc*:*aa*$_3$ oxidase[18]. The catalytically active subunits that contain their cofactors within the cyt-*aa*$_3$ domain are CtaC and CtaD. CtaC is a transmembrane protein with the covalently bound Cu_A (Fig. 2B) that receives electrons from the cyt-*bcc* domain. CtaD with the co-factors heme *a*, heme *a*$_3$ and Cu_B in the central cavity adopts a barrel-like arrangement comprising of 12 TMHs (Fig. 2B, Supplementary Figs. 2, 3).

Mab cyt-*bcc*:*aa*$_3$'s canonical electron- and proton pathways

The canonical electron pathway observed in *Mtb* (PDB: 8HCR, 7E1V, 7E1W and 7E1X) and *M. smegmatis* (PDB: 6ADQ, 6HWH, 7RH5, and 7RH7) is conserved in the *Mab* cyt-*bcc*:*aa*$_3$ oxidase. The redox potential guided spatial mycobacterial organisation of the cofactors generates a redox potential gradient in the supercomplex, for efficient electron transfer and protection against short-circuits in the multifunctional supramolecular assembly (Fig. 3A). The distinct coulombic densities for MQH_2/menaquinone (MQ), at the Q_o sites and Q_i sites, (Supplementary Fig. 4), illuminated the bifurcated electron pathway and highlighted the strong interaction with neighbouring residues in the vicinity (Fig. 3B). The current resolution does not allow for the clear distinction between MQH_2 and MQ thus requiring the need to rely on the spatial arrangement at the active sites to predict the most likely candidate observed. Under physiological conditions, efficient transfer of electrons is hindered when the distance extends beyond 14 Å[19]. In the Q_o site, the edge-to-edge distance from the electron carrier to heme b_L is 19 Å which exceeds the 14 Å limit for efficient physiological electron transfer. Furthermore, recent cryo-EM studies found Q203 to bind deeper within the Q_o site, suggesting that the endogenous electron donor MKH_2 occupies a deeper position within the pocket for efficient electron transfer[15,20]. This implies that the density observed in the Q_o site would most likely correspond to an oxidized product leaving the active site. On the other hand, the density for the electron carrier at the Q_i site, is 9 Å away from heme b_H allowing for efficient electron transfer. This suggests that the density observed in the Q_i site would most likely correspond to either MQ or partially reduced semi-MQ. MQ molecules were also resolved in interfaces between the QcrC membrane domain and QcrB suggesting a potential role maintaining the structural integrity of the enzyme[11]. The binding of the substrate MQH_2 14 Å away from the [2Fe-2S] cluster allows for a rapid transfer of the first electron to the cofactor, which then follows the increasing redox potential gradient towards the final acceptor: [2Fe-2S] <cyt-c_I <cyt-c_{II} < Cu_A <Heme *a* <Heme *a*$_3$ < O_2 (Fig. 3B). The second electron from the semiquinone is transferred to the low potential heme b_L located 19 Å away (Fig. 3C). The electron from heme b_L is transferred via L222 to the high potential heme b_H (14 Å distance), to a bound MQ at the Q_i site to allow for the generation of MQH_2 and establishment of the Q-cycle (Fig. 3C).

The understanding of the Q-cycle within the *Mab* cyt-*bcc* domain was further enhanced through the visualization of the proton uptake and release pathways. The proton entry site begins from a cardiolipin molecule located at the entrance of a cavity between the cyt-*bcc* and cyt-*aa*$_3$ domain (Fig. 3D). A network of water molecules connects the entrance subunit QcrB residue K262, where the proton from the chargeable residue is acquired by E46 and is transferred to the bound menaquinone through a water molecule mediated H-bond (Fig. 3D). The structure revealed two proton release pathways similar to those seen in *Corynebacterium glutamicum*[21]. The first proton exit pathway is aligned with protonatable QcrB amino acids D311, R315, D304, and QcrC residue E272, located in the vicinity of a water channel and allowing proton translocation via a Grotthuss transport mechanism[22] and an QcrA and QcrB interface to the periplasmic region (Fig. 3D). The second proton exit pathway begins with the protonatable D396 and extends to the periplasmic region via a network of water molecules (Fig. 3D).

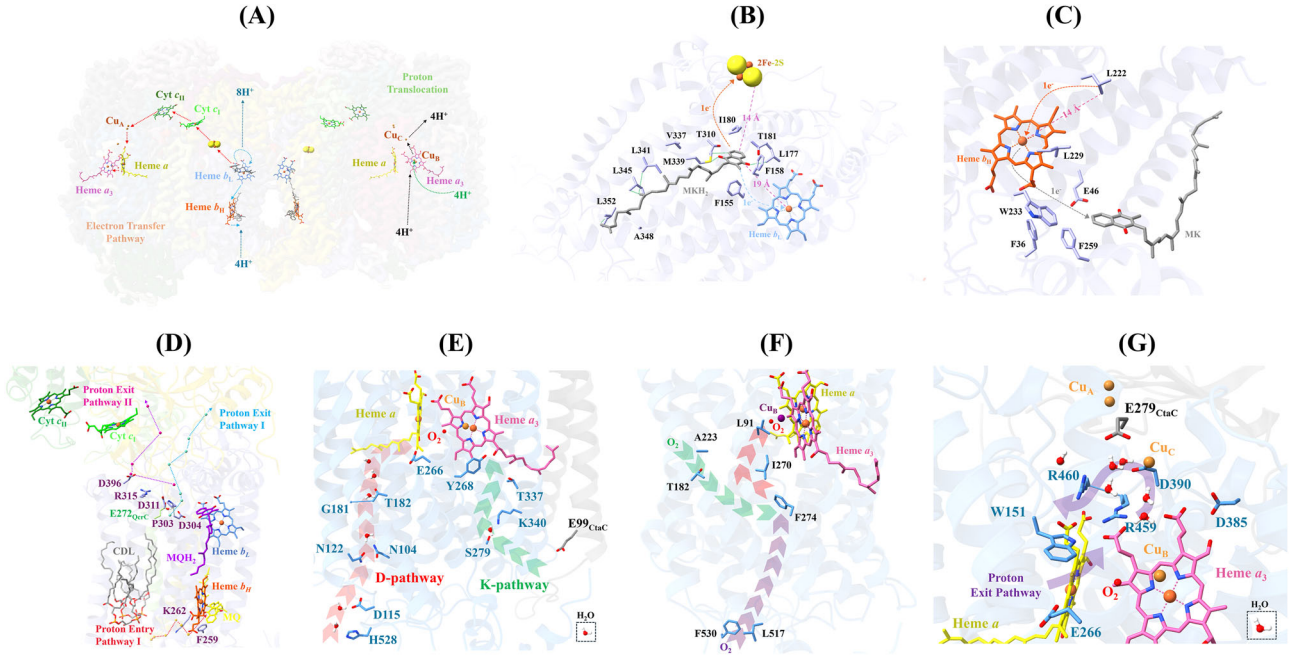

Fig. 3 | Reaction centers and substrate pathways of the *M. abscessus* cyt-*bcc*:*aa*$_3$ supercomplex. A Electron transfer and proton translocation pathways. **B** Architecture of MQH_2-binding site (**C**) Architecture of MQ-reduction site. **D** Proton entry and exit pathways in cyt-*bcc*. **E** D- and K-pathways in cyt-*aa*$_3$. **F** Proposed Y-shaped Oxygen channel in ctaD. **G** Proton exit pathway in cyt-*aa*$_3$.

H^+-translocation towards the binuclear centre occurs via a Grotthuss mechanism

The H^+-conducting D-pathway is formed by the CtaD residues N104, D115, N122, G181, T182 and E266. In contrast, the K-pathway is formed by CtaC residue E99, as well as the CtaD amino acids S279, T337 and K340 (Fig. 3E). The pathways formed by hydrophilic residues revealed the presence of water molecules in the immediate vicinity illustrating a proton-transported based on the Grotthuss mechanism towards the binuclear centre (BNC) formed by Cu_B and Fe (Heme a_3) (Fig. 3E). The BNC is in proximity to a dioxygen molecule located in a hydrophobic pocket formed by CtaD non-polar amino acid (W151, W260, V267 and L91). The dioxygen in *Mab* occupies an equivalent position as described in the *C. glutamicum* SC structure (PDB:7QHO[21]), giving further confidence to the assignment.

The transport of dioxygen to the BNC is hypothesised to occur via a hydrophobic Y-shaped oxygen diffusion pathway which has close resemblance to the *T. thermophilus* cytochrome *c* oxidase[23]. The pathway has two entrances formed by T182/A223 and L517/F530 (Fig. 3F). The channels extending from both the entrances converge at F274 and continue via I270 and L91 to reach the heme a_3 reaction center for the reduction of oxygen to water (Fig. 3F). The catalytic domain, which reduces oxygen to water, is also involved in the translocation of electrons to the electropositive membrane side. The exit route for the protons from the D-pathway, previously described in the *C. glutamicum* oxidase structure (PDB:7QHO[21]), was captured in the *Mab* cyt-*bcc*:*aa*$_3$ oxidase. Residue E266, which serves as the gating residue, acquires protons from the D-pathway and passes them to R459 via the guanidino group (Fig. 3G). The presence of a water network highlights the utilisation of the Grotthuss mechanism for efficient sequential proton transfer to D390, and the exiting proton leaves the domain via an exit formed by R460 and CtaC residue E279 (Fig. 3G).

Residues responsible for Q203 inactivity in *Mab*

The recently resolved Q203-bound- and apo *Mtb* cyt-*bcc*:*aa*$_3$ structures revealed the residues within the substrate-binding pocket being involved in inhibitor-binding and undergoing movements[3] (Fig. 4A–C). In particular the QcrB residues S304, T313, E314 and A317 interacting with the imidazo[1,2-*a*]pyridine (IP) moiety undergo major movements due to Q203-binding (Fig. 4C). Importantly, the cavity formed by the *Mtb* residues S304, E314 and A317 is smaller in the presented *Mab* structure, where E314 and A317 are substituted by the *Mab* residues D311 and L314 (Fig. 4B). The superimposition of the *Mtb* Q203-binding conformation in the *Mab* structure (r.m.s.d 0.4 Å) shows that D311 is angled approximately 130° anti-clockwise away from the nitrogen at position 2 compared to *Mtb* E314 (Fig. 4D). This causes the residue to be within a 1.9 Å proximity to the nitrogen suggesting possible steric hinderance. Even a 1 Å shift during Q203-binding observed for *Mtb* E314, would not be sufficient to avoid steric interactions in the *Mab* D311 residue (Fig. 4D).

To test, whether substitutions of an E to D and A to L in the *Mab subsp. abscessus* enzyme cause the loss of Q203 potency, the *Mab* residues D311 and L314 were mutated to the *Mtb* variants to obtain the *Mab* cyt-*bcc*:*aa*$_3$ oxidase double mutant *Mab* D311E/L314A (Supplementary Table 8). To rule out that the mutations may alter the overall oxygen consumption, a qualitative Methylene blue assay was performed (Supplementary Fig. 5A). As demonstrated in Fig. 5A, the D311E/L314A mutant was susceptible to Q203 at nanomolar range in growth inhibition and whole cell ATP akin to the quadruple G179S/D311E/L314A/C393A mutant, described to retain Q203-sensitivity based on the natural polymorphisms[14]. The effect of the *Mab* D311E/L314A variant on whole cell respiration was determined using the Seahorse XFe96 platform, where Q203 induced the characteristic initial spike in the oxygen consumption rate (OCR) like the profile observed in *Mtb* (Supplementary Fig. 5B, C). In contrast, no oxygen consumption effect could be observed in the WT *Mab*, which underscores the critical role of D311 and L314 in preventing Q203-binding to the *Mab* cyt-*bcc*:*aa*$_3$ oxidase (Supplementary Fig. 5D). To confirm that the drug sensitivity is mainly related to the D311E/L314A substitutions and to narrow down the residue most relevant for Q203-binding, the single mutants G179S, D311E and C393A were designed. The efficacy of Q203 remained unchanged in the G179S and C393A distal mutants in both the growth inhibition and whole cell ATP synthesis assays, reflecting that G179 and C393 are not related to Q203's inactivity

https://doi.org/10.1038/s41467-026-70805-5

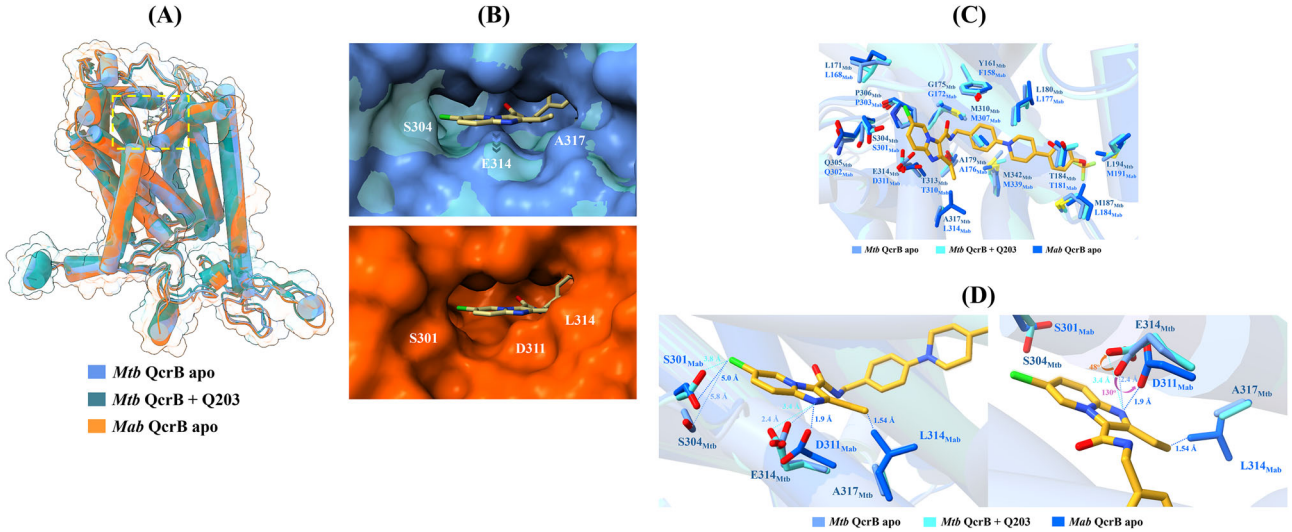

Fig. 4 | Structural investigation of the Q203-binding pocket in QcrB. **A** Superimposition of the *Mtb* apo (blue, PDB: 7E1V), *Mtb* Q203-bound (turquoise, PDB: 7E1W) and *Mab* apo (orange) QcrB subunits reveals a conserved architectural arrangement. **B** Investigating the Q203-binding pocket surfaces of the *Mtb* apo (blue, PDB: 7E1V), *Mtb* Q203-bound (turquoise, PDB: 7E1W) and *Mab* apo structures (orange). **C** Amino acids with close interactions to Q203 in *Mtb* apo (blue, PDB: 7E1V), *Mtb* Q203 bound (cyan, PDB: 7E1W), and *Mab* apo structures (cornflower blue). **D** Amino acid orientation of key residues with close interactions to Q203 in *Mtb* apo (blue, PDB: 7E1V), *Mtb* Q203 bound (cyan, PDB: 7E1W), and *Mab* apo structures (cornflower blue).

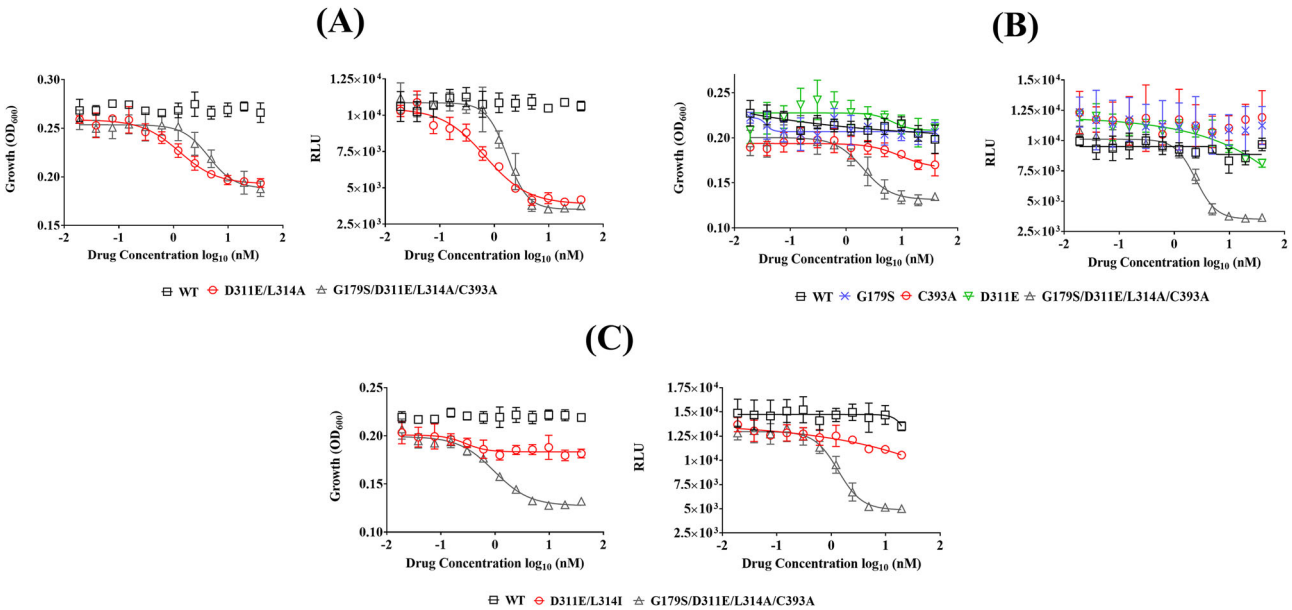

Fig. 5 | Identification of the key residue responsible for the inactivity of Q203 in *Mab*. **A** Growth inhibitory and ATP depletion activity of Q203 in *Mab* WT (black open square), *Mab* D311E/L314A (red open circle) and *Mab* G179S/D311E/L314A/C393A (grey open upward triangle). Q203 activity was restored in the *Mab* D311E/L314A mutant akin to the G179S/D311E/L314A/C393A quadruple mutant. **B** Growth inhibitory and ATP depletion activity of Q203 in *Mab* WT (black open square), *Mab* G179S (blue cross), C393A (red open circle), D311E (green open downward triangle) and G179S/D311E/L314A/C393A (grey open upward triangle). In both assays, Q203 was inactive in all single mutants except for the D311E mutant where partial activity was restored. **C** Growth inhibitory and ATP depletion activity of Q203 in *Mab* WT (black open square), *Mab* D311E/L314I (red open circle) and *Mab* G179S/D311E/L314A/C393A (grey open upward triangle). The D311E/L314I mutant was unable to restore the activity of Q203 completely in comparison to the D311E/L314A and G179S/D311E/L314A/C393A mutants. All data are presented as mean values ± SD from $n = 3$ biological replicates. Source data are provided as a Source Data file.

(Fig. 5B). In comparison, the D311E mutant sensitized the strain in part towards Q203 (Fig. 5B). However, the inhibitory effect of Q203 against the D311E mutant was not as drastic compared to the *Mab* D311E/L314A double mutant, indicating that the reduction in the *Mab* cyt-*bcc*:*aa*$_3$ cavity volume (Fig. 4B) caused by L314 plays a key role in disrupting inhibitor-binding. The close distance (1.5 Å) of L314 from the ethyl at position 2 of the IP moiety revealed in Fig. 4D illustrates the steric hinderance experienced by the drug.

Interestingly, the corresponding residue in *Mycobacterium smegmatis* is isoleucine, compared to the *Mab* L314 and the *Mtb* alanine, which correlates with Q203 being 100-times less effective against *M. smegmatis* than *Mtb*[10]. Generating and characterizing a *Mab* cyt-*bcc*:*aa*$_3$

https://doi.org/10.1038/s41467-026-70805-5

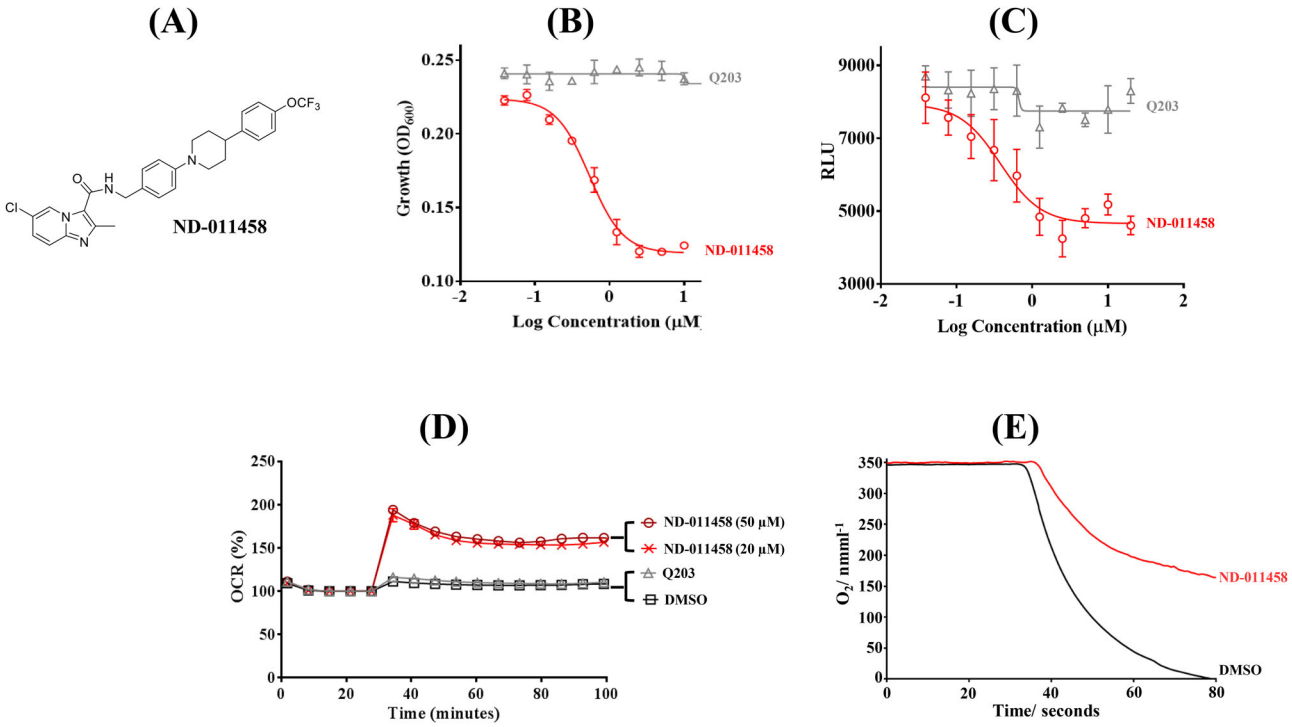

Fig. 6 | Structure-based drug design and characterization of putative *M. abscessus* cyt-*bcc*:*aa*$_3$ inhibitors. A Design of Q203 analog with modification at position 1. **B** Growth inhibitory activity of ND-011458 (red circle) and Q203 (grey triangle) in *Mab* subsp. *abscessus* (R). ND-011458 exhibited activity against subsp. *abscessus* resembling the profile of Q203 in the D311E/L314A and G179S/D311E/L314A/C393A, while Q203 were inactive. Data are presented as mean values ± SD from $n = 3$ biological replicates. **C** ATP depletion activity of ND-011458 (red circle) and Q203 (grey triangle) in *Mab* subsp. *abscessus* (S). ND-011458 depleted whole cell ATP levels in *Mab* subsp. *abscessus* (S) resembling the profile of Q203 in the D311E/L314A and G179S/D311E/L314A/C393A mutants. Data are presented as mean values ± SD from $n = 3$ biological replicates. **D** Real-time monitoring of respiration in the presence of ND-011458 (50 μM, Maroon circle; 20 μM, red cross), Q203 (grey triangle) and DMSO (Black square) using Seahorse XFe96 Extracellular flux analyzer in *Mab* subsp. *abscessus* (S). ND-011458 was able to achieve the characteristic respiratory burst observed for Q203 in *Mtb* due to the electron flux being rerouted to cytochrome *bd* oxidase, which consumes oxygen at a higher rate compared to the baseline. **E** ND-011458 (red line) inhibited respiration in the purified recombinant *Mab* subsp. *abscessus* cyt-*bcc*:*aa*$_3$ supercomplex compared to the vehicle control, DMSO (black line). Source data are provided as a Source Data file.

D311E/L314I mutant resulted in a reduced Q203-effect in both whole cell ATP formation (Fig. 5C) and oxygen consumption rates (Supplementary Fig. 5E), when compared to the D311E/L314A mutant, indicating the critical role of the *Mtb* alanine residue in Q203 inhibition when compared to the isoleucine and leucine in *M. smegmatis* and *Mab*, respectively.

Structure-based design of ND-011458, a *Mab* complex cyt-*bcc*:*aa*$_3$ oxidase inhibitor

The steric hinderance associated with the 'blockade' effect caused by *Mab* QcrB residue L314, which is not present in other pathogenic mycobacterial species (Supplementary Fig. 6), inspired a hit identification attempt where the ethyl group at position 2 in the imidazo[1,2-a] pyridine (IP) core was shortened to a -methyl, leading to the generation of the analogue ND-011458 (Fig. 6A; see Supplementary Information: *General synthesis routes to compounds*). The analogue was validated in a growth inhibitory assay where ND-011458 inhibited the growth and ATP formation of the smooth (S) or rough (R) morphotypes of *Mab* subsp. *abscessus* with an MIC_{50} of 539 ± 36 nM and 438 ± 34 nM as well as an IC_{50} of 381 ± 99 nM and 381 ± 99 nM, respectively (Fig. 6B, C, Supplementary Fig. 7, Supplementary Table 9). The effect of the analogue on whole cell respiration in *Mab* subsp. *abscessus* mirrored a profile of Q203 in *Mtb* (Fig. 6D) where an increase in oxygen consumption rate (OCR) is observed upon the addition of the inhibitor[24]. This phenomenon is attributed to the electron flux being rerouted to cytochrome *bd* oxidase which consumes oxygen at a higher rate[24]. The specificity of ND-011458 for the *Mab cyt-bcc*:*aa*$_3$ was determined next with the recombinant *Mab* cyt-*bcc*:*aa*$_3$ oxidase, where ND-011458 reduced respiration levels compared to the vehicle control (Fig. 6E). Together with the subspecies *Mab* subsp. *bolletii* and *Mab* subsp. *massiliense*, *Mab* subsp. *abscessus* belongs to the so-called *Mab* complex, which show different drug susceptibilities[11]. Supplementary Table 9 shows that the compound also displayed high efficacy against *M. bolletii* and *M. massiliense* with MIC_{50} of 312 ± 64 nM and 637 ± 76 nM, respectively, indicating that the inhibitor is active against the three subspecies of the *Mab* complex.

To confirm and visualize ND-011458-binding to the enzyme, the cryo-EM structure of the ND-011458-bound *Mab* subsp. *abscessus cyt-bcc*:*aa*$_3$ oxidase was resolved at 2.26 Å resolution (Fig. 7A–D; Supplementary Fig. 8). The inhibitor density was observed in the Q_o-binding pockets of both monomeric units, with the absence of any large-scale conformational changes to the overall oxidase structure (Fig. 7A). The inhibitor density allowed for the imidazopyridine moiety, amide linker region, and A-phenyl and B-piperidinyl moieties to be resolved clearly while the end of the tail, which extends towards the lipid bilayer, could not be resolved well due to weaker density in the region (Fig. 7A). The IP moiety binds deep in the Q_o-binding pocket, being 7 Å and 12.7 Å away from the FeS-cluster and Heme b_L, respectively (Fig. 7B), adopting a binding conformation similar to menaquinol forming multiple interactions with the QcrA and QcrB subunits. The resolved inhibitor-enzyme complex structure revealed residues close to ND-011458: F158, Y161, L168, G172, A176, L177, T181, L184, M191, S301, Q302, P303, M307, T310, D311, L314 and M339 (Fig. 7A, C, D). The binding conformation preserves the hydrogen bond interaction between subunit QcrA residue H338 and the N1 nitrogen in the imidazopyridine moiety, as seen for Q203. This interaction, which is

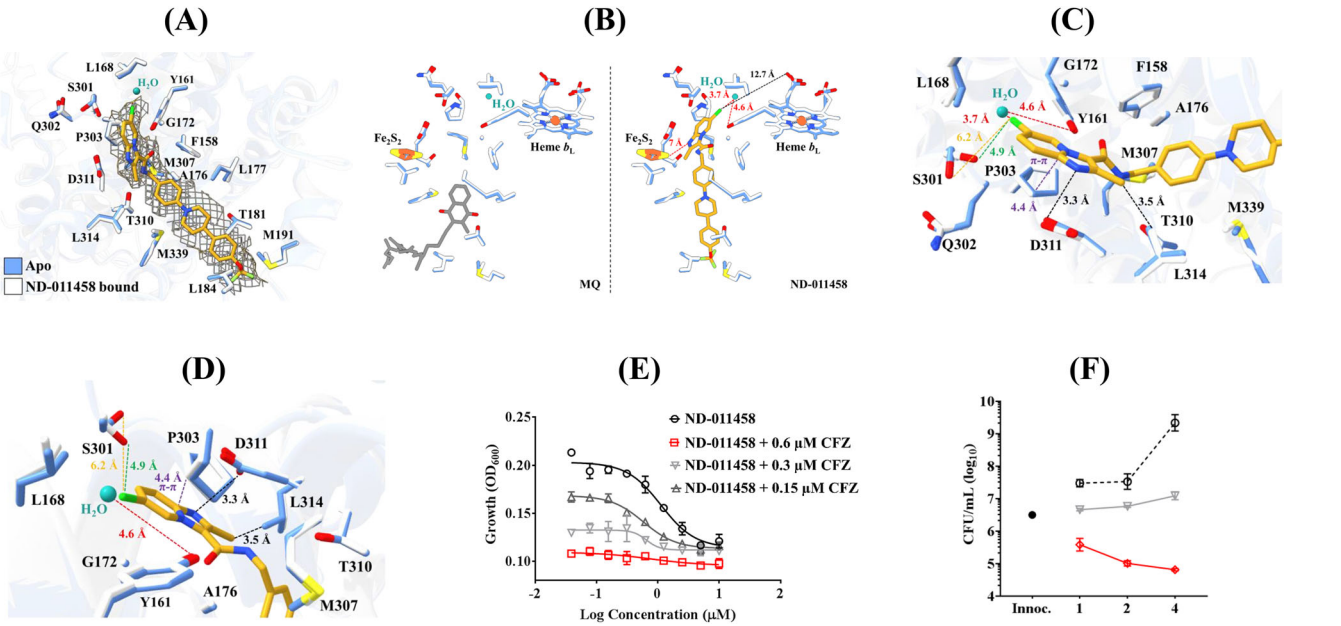

Fig. 7 | ND-011458 bound *Mab* subsp. *abscessus* cyt-*bcc*:*aa*$_3$ cryo-EM structure. **A** Cryo-EM map revealed an apparent density of ND-011458 in the MQ binding pocket interacting with several key residues, which adopt similar positions in both the apo (blue) and inhibitor-bound (white) structures. **B** ND-011458 binds deeper in the MQ binding pocket, blocking the entry of substrate MQs, thereby disrupting rapid electron transfer to the Fe_2S_2 cluster and Heme b_L. **C** Key interactions between the Imidazopyridine amide (IPA) core in the MQ binding pocket. **D** Bridging water molecule connecting Y161 and the chloride moiety from the IPA core. **E** Enhanced potency of ND-011458 in combination with Clofazimine (CFZ). **F** Bactericidal activity of ND-011458 [10 μM] in combination with CFZ [8 μM] against *M. abscessus* CIP104536^T (red diamond) over 4 days with dimethyl sulfoxide (DMSO) serving as the vehicular control (black open circle) and CFZ alone (8 μM) serving as the negative control (grey triangle). Bacterial viability was determined by enumerating CFU on lysogeny broth (LB) agar plates on days 1, 2, and 4. The dotted lines represent the limit of detection. ND-011458 in combination with CFZ was bactericidal, reducing the bacterial load by approximately 1.5 log in 4 days, while the CFZ control remained bacteriostatic. All experiments were performed in triplicate and repeated at least once. The data are expressed as the means ± standard deviations of triplicates for each condition. Source data are provided as a Source Data file.

also observed for ubiquinol, is proposed to coordinate the Q-cycle in $CIII_2$[25]. The methyl group at position 2 of the IP moiety establishes hydrophobic interactions with subunit QcrB residues A176 and L314 located 4 Å and 3.5 Å away respectively, while the 6-chloro group, being 3.5 Å away from the backbone carboxyl group of QcrB L168, potentially forms a halogen bond (Fig. 7C, D). The amide linker was found to preserve the key interaction with T310 located 3.7 Å away, which is crucial for the activity of Q203 in *Mtb* (Fig. 7B)[15]. The A-phenyl group, which is positioned similar to the MQ head group, established π-π interaction with F158 allowing for an aromatic interaction between the target and inhibitor and suggesting an effective blockade to prevent the entry of substate molecules for the transfer of electrons to the catalytic center (Fig. 7D). The high-resolution density map also revealed the presence of a bridging water molecule between the IP core and Y161, highlighting intricate networks required for the stability of the inhibitor in the cavity (Fig. 7A, C, D).

To reduce the viability of *Mab*, the OXPHOS pathway has been demonstrated to be a druggable complex with modulators such as clofazimine (CFZ[26]), proposed to compete with the mycobacterial specific electron acceptor menaquinone for its reduction by the NDH-2 complex[16] and circumventing respiration by shuttling electrons from NADH directly to oxygen or the F-ATP synthase inhibitors BDQ[27], TBAJ-876[28], TBAJ-5307[29], GaMF1[30] or SQ31f[31]. The treatment of *Mab* infections typically requires a combination of drugs. Recently, it has been demonstrated that Q203 or its analog TB47 does not potentiate the efficacy of CFZ against *Mab*[32]. Here, we investigated the interaction of ND-011458 with CFZ. As revealed in figure 8E, CFZ reduced the MIC_{50} of ND-011458 in a concentration-dependent manner. The checkerboard assay demonstrates an additive growth reduction by the combination of CFZ and ND-011458 (Fig. 7E; Supplementary Fig. 9A), achieving a minimum fractional inhibitory concentration (FIC) index of 0.82 (Supplementary Table 10). Interestingly, the bactericidal anti-TB agent CFZ is bacteriostatic in *Mab*. Given the additive relationship between CFZ and ND-011458 (Fig. 7F), the ability of ND-011458 to modulate the potency of CFZ was investigated in a kill kinetics study. The potent combination elicited a strong response, resulting in a 1 log decrease in colony-forming units (CFU) counts within just 4 days of treatment (Fig. 7F), making these dual inhibitors an attractive anti-*Mab* combination.

The present study reports the successful host expression, isolation, and purification of a functional *Mab* cyt-*bcc*:*aa*$_3$, enabling its cryo-EM structure to be resolved at 2.6 Å. The structure reveals the electron, proton, and oxygen transfer pathways that drive oxygen reduction and proton motive force generation, underscoring their essential role in mycobacterial energy metabolism and their potential as novel antibacterial target space. Comparative structural analysis across *Mtb*, *M. smegmatis*, and *Mab* defined the evolution of the QcrB substrate-binding cavity and identified residue L314 as the primary determinant of Q203 potency in *Mab*. Guided by these insights, we designed ND-011458, a QcrB inhibitor with high potency against *Mab* growth. The 2.26 Å inhibitor-bound structure confirms the substrate-binding site as the compound target and reveals deep penetration into the binding pocket near the FeS cluster and low-spin heme b_L, blocking electron transfer to both reaction centres and disrupting oxygen reduction and MHQ_2 regeneration (Supplementary video). ND-011458 also enhanced *Mab* growth inhibition and killing activity when combined with CFZ. This potent bactericidal combination opens a new avenue for developing dual-inhibitor regimens. Together, these findings provide a structural and mechanistic framework for QcrB inhibitor design in the *Mab* complex and establish a foundation for future campaigns targeting mycobacterial respiratory complexes.

Methods

Generation of *Mab* with genomic cyt-*bcc*:*aa*$_3$-FLAG/6×HIS tag

The mycobacterial shuttle vector pKM444 was first electroporated into wild-type (WT) *Mab*. The resulting *Mab*::pKM444 strain was selected on 7H10 complemented with oleic-acid-dextrose-catalase (OADC) plates, supplemented with 50 µg/mL kanamycin. Colonies were expanded and grown to an optical density at 600 nm (OD_{600}) of 0.1 before induction with 1 µg/mL anhydrotetracycline. The culture was induced again at OD_{600} = 0.5 for 24 h to express the Che9c phage RecT annealase and the Bxb1 phage integrase. A modified payload plasmid pKM 491 M was generated for this study from pKM 491 where the Hygromycin cassette was swapped with a zeocin cassette[17]. The induced strain was washed in 0.05% Tween 80 at room temperature three times and finally resuspended to OD_{600} = 100, before being coelectroporated with 200 ng of pKM 491 M and 1 µg of targeting oligonucleotide 5′ -CGA ACA ACG TGC CCT TGC CGC ACT GCG CGA ACA CCA GGA CAG CAT CAT GGG TTC GCC AGA CGG CGA GCA CGG TTT GTC TGG TCA ACC ACC GCG GTC TCA GTG GTG TAC GGT ACA AAC CTG ACC CGG CGA CGA CCC GGG TCG GCA CGA CCC GGG AAG GAA CCG GGC AAA TCA AGC ACA GCC CGG CGA CGA CC-3′. The electroporated cells were recovered overnight in 7H9-albumin-dextrose (ADS) culture broth medium. The recombinant strain was selected on 7H10-OADC plates, supplemented with 50 µg/mL hygromycin. The strain was validated by PCR with the forward primer 5′ -CAC CAT TGA TGA CTC GAG TCT AGA GCA TG-3′ and the reverse primer 5′-ATG ATG GTG GTG GTG GTG GTG GTG-3′. The expression of the FLAG tag was validated by Western blotting.

Western blot validation of genomic FLAG tag

First, 1 mL of the culture strain (OD_{600} = 1) strain, containing the FLAG genomic tag, was sonicated for 1 min at 30% power using Bandelin Sonopuls (Bandelin, Berlin, Germany) for five cycles. The sonicated sample was centrifuged at 12,000 rpm. The supernatant was applied to a 12% SDS gel and transferred to a nitrocellulose membrane using a semidry transfer apparatus according to the manufacturer's protocols (Carl Roth, Karlsruhe, Germany). After blocking with 3% gelatin in a TBSN-Tween buffer (20 mM Tris-HCl [pH 7.5], 500 mM NaCl, 0.02% NaN3, and 0.05% Tween 20) for 1 h at room temperature, the membrane was washed with 1% gelatin in TBSN-Tween for 3 × 10 min. Afterward, the membranes were incubated with a rabbit anti-FLAG HRP-conjugated antibodies against the FLAG tag (Abcam, Cambridge, United Kingdom) diluted (1:2000) with 1% gelatin TBSN-Tween 20 for 1 h at room temperature, followed by three washing steps (15 min) with TBSN-Tween 20 buffer. The antibodies were detected using SuperSignal West Pico Plus chemiluminescent substrate according to the manufacturer's protocol (Thermo Fisher Scientific, Waltham, MA).

Purification of *Mab* cyt-*bcc*:*aa*$_3$ oxidase

The strain containing the genomic tag was grown in 7H9-ADS-glycerol medium until reaching an OD_{600} of 2.0 to 2.5. Cell pellets were harvested and stored in −80 °C. Then, 10 g of cell pellets was dissolved in 100 mL of buffer A (20 mM MOPS [pH 7.4], 100 mM NaCl, 2 mM Pefabloc, 1 mM PMSF, 10% glycerol) and briefly sonicated in ice to ensure complete resuspension. Cell lysis was achieved by three passes through a microfluidizer (Microfluidics, Newton, MA) at 4 °C and 1.2E + 8 Pa. The lysate was centrifuged at 18,000 x g for 20 min to remove cell debris and unlysed cells. The resulting supernatant was centrifuged at 165,000 x g for 1 h in a P50AT2 rotor (Hitachi Himac Ultracentrifuge; Eppendorf Himac Technologies Co., Ltd., Japan). The membrane pellets from the previous step were resuspended in buffer B (20 mM MOPS [pH 7.4], 100 mM NaCl, 2 mM Pefabloc^{SC}, 1 mM phenylmethanesulfonyl fluoride (PMSF), 1% [wt/vol] n-dodecyl-β-D-maltoside (DDM), 10% glycerol). The mixture was stirred for 1 h at 4 °C on a rotating wheel. After solubilization with the detergent, the mixture was centrifuged at 39,500 x g for 30 min at 4 °C. The supernatant was allowed to equilibrate with 1 mL of FLAG beads for 1 h; the resin was then washed with buffer C (20 mM MOPS [pH 7.4], 100 mM NaCl, 2 mM Pefabloc, 1 mM PMSF, 0.01% [wt/vol] DDM). The protein was eluted with buffer D (20 mM MOPS [pH 7.4], 100 mM NaCl, 2 mM Pefabloc, 1 mM PMSF, 0.01% [vol/wt] DDM, 100 µg/mL 3xFLAG). Protein samples that were collected during the course of the experiment were analyzed using 12% SDS-PAGE. Bands of the SDS PAGE were verified by MALDI-TOF (SBS Biosciences Research Centre, NTU).

MALDI-TOF Analysis

The Mass Spectrometry experiments were performed in the Mass Spectrometry Core Facility in the School of Biological Sciences, Nanyang Technological University. The peptide sample was mixed with an equal amount of matrix solution containing 10 mg/mL R-cyano-4-hydroxycinnamic acid in 0.1% trifluoroacetic acid (TFA)/ 50% acetonitrile (ACN) and spotted onto a 384-well stainless steel MALDI target plate (Applied Biosystems, Foster City, CA). An ABI 4800 Proteomics Analyzer MALDI TOF/TOF mass spectrometer (Applied Biosystems) was used to analyze the spotted samples. Both MS and MS/MS spectra were recorded in the combination mode and submitted for database searching. For protein ID, combined MS and MS/MS data were submitted via GPS Explorer (version 3.6, Applied Biosystems) to Mascot server (version 2.0, Matrix Science) for database searching. Mascot algorithm was then used for data searching to identify proteins using the following parameters; missed cleavage of two; dynamic modifications were oxidation (+15.995 Da) (M), The static modifications was Carbamidomethyl (+57 Da) (C).

Heme absorbance spectra of purified *Mab* cyt-*bcc*:*aa*$_3$

The spectra were analyzed using an Amersham Biosciences Ultrospec 2100 Pro UV-Visible absorption spectrophotometer (Amersham, Piscataway, NJ). The spectra were recorded over a wavelengths ranging from 400 to 700 nm. The purified *Mab* cyt-*bcc*:*aa*$_3$ at a concentration of 1 mg/mL was oxidized with 100 µM potassium ferricyanide. The oxidized UV spectra were subsequently recorded. The sample was reduced using 100 mM sodium dithionite. The reduced UV spectrum was recorded promptly. The difference spectra were then obtained by subtracting the absorbance value of the reduced state from that of the oxidized state. The difference spectra were plotted using GraphPad Prime 8.0 software[33].

2,3-Dimethyl-1,4-naphthoquinol oxygen consumption assay

20 mM DMNQ (Enamine, Cincinnati, OH) was prepared in 1 mL of ethanol containing 6 mM HCl. The DMNQ solution was reduced with a few grains of sodium borohydride ($NaBH_4$) in an ice bath. Then, 10 µL of 12 N HCl was used to quench the reaction. This reaction resulted in the formation of $DMNQH_2$. A serial 2-fold dilution of the 20 mM $DMNQH_2$ solution, in absolute ethanol, was performed till a 2.5 mM solution of $DMNQH_2$ was obtained to minimize the presence of $NaBH_4$ in the final solution. The oxygen consumption assay was performed based on published protocols[3–5]. Briefly, a 1 mg/mL stock of the purified *Mab* cyt-*bcc*:*aa*$_3$ oxidase was resuspended in 500 µL of reaction buffer (20 mM MOPS [pH 7.4], 100 mM NaCl, 0.01% DDM) to a final concentration of 65 nM and added into the reaction chamber. The baseline was monitored using a Clark-type oxygen electrode (Oxytherm+, Hansatech, Pentney, United Kingdom) for 50 s. 5 µL of 2.5 mM $DMNQH_2$ was then injected into the reaction chamber to achieve a final $DMNQH_2$ concentration of 25 µM and initiate respiration within the oxidase. The reaction chamber was immediately sealed, and oxygen consumption was monitored till a plateau was achieved. The oxygen consumption curves were plotted using GraphPad Prime 8.0 software[33].

Cryo-EM data collection and processing

The purified *Mab* cyt-*bcc*:*aa*$_3$ was concentrated to 13 mg/mL. Portions (4 µL) of the sample were applied to glow-discharged Quantifoil R1.2/1.3 holey carbon grids. The grids were blotted for 2 s at 100% humidity and 4 °C and plunge-frozen using a FEI Vitrobot Mark IV (Thermo Fisher Scientific). Images were taken using an FEI Titan Krios electron microscope operating at 300 kV with a K3 Summit detector (Gatan, Pleasanton, CA) at a magnification of ×130,000. Images were recorded in super-resolution mode. Automated single-particle data acquisition was performed using EPU software. A defocus range of 1.0 to 2.0 µm was implemented. Movies were collected at 40 frames per stack with an exposure time of 2.83 s. The total dose was set at 56 $e^-/Å^2$. Motion correction was performed using MotionCor2 and CTF estimation was performed using CTFFind4[34,35]. The data processing was performed on CryoSPARC[36,37]. Structure refinement was done using COOT and Phenix software[38,39].

In the case of *Mab* cyt-*bcc*:*aa*$_3$ complexed with ND-011458, the FLAG elution was incubated with 50 µM of ND-011458 (2.5% DMSO) for 30 min in ice. The eluant was then concentrated to 8.2 mg/mL. The grid freezing was performed as mentioned for the apo-protein. Images were taken using an FEI Titan Krios electron microscope operating at 300 kV with a K3 Summit detector (Gatan, Pleasanton, CA) at a magnification of ×165,000. Images were recorded in super-resolution mode. Automated single-particle data acquisition was performed using EPU software. A defocus range of 0.5 to 1.5 µm was implemented. Movies were collected at 40 frames per stack with an exposure time of 2.83 s. The total dose was set at 60 $e^-/Å^2$. Motion correction was performed using MotionCor2 and CTF estimation was performed using CTFFind4[34,35]. The data processing was performed on CryoSPARC[36,37]. Structure refinement was done using COOT and Phenix software[38,39].

Model building and refinement

The atomic model of the cytochrome cyt-*bcc*:*aa*$_3$ oxidase was built in using the automated protein structure homology-modelling server SWISS-MODEL using the PDB model of the cytochrome cyt-*bcc*:*aa*$_3$ oxidase from *M. smegmatis* (6ADQ) as reference structure[3,40]. Thereafter, manual backbone tracing and docking of side chains in the respective map densities was done before performing real-space refinement in Phenix (version 1.20.14487)[39]. The refinement results were used to manually inspect and corrected the structures accordingly. The finalized model was validated by the MolProbity online server[41]. Map-to-model cross validation was performed in Phenix (version 1.20.14487). $FSC_{0.5}$ was used as cutoff to define resolution. The water molecules present in the structures were modelled based on the high-resolution cryo-EM structure of the *Corynebacterium glutamicum* cyt-*bcc*:*aa*$_3$ supercomplex[21]. ND-011458 was modelled by modifying Q203 from the ligand ID HUU. A summary of the model parameters and the corresponding cryo-EM map statistics is found in Supplementary Table 6-7. The finalized model was visualized using ChimeraX[18].

Design and expression of *Mab* cyt-*bcc*:*aa*$_3$ mutants

The *Mab qcrCAB* operon including its native promoter (330 bp upstream of the coding region) was synthesized by Bio Basic Asia Pacific Pte. Ltd, Singapore and incorporated into the pMV306 vector to yield the plasmid pMV306::*Mab_qcrCAB*[14]. The resulting plasmids, pMV306::*Mab_qcrCAB*, served as templates for downstream mutations. Site directed mutagenesis were performed using the primers listed in Supplementary Table 3. The Q5 High-Fidelity (New England Biolabs) and KAPA HiFi HotStart PCR Kits (Roche Sequencing Solutions) were used according to the manufacturer's instructions. Successful site directed mutagenesis of the target nucleotides was confirmed by Sanger sequencing. The plasmids carrying desired mutations was transformed into *Mab* Δ*qcrCAB* (Δ*bcc*) strain by electroporation. Colonies were selected on 7H10 agar plates supplemented with 10% OADC, zeocin (20 µg/mL) and kanamycin (50 µg/mL).

Minimum inhibitory concentration (MIC) determination

Mab subsp. *abscessus* CIP104536^T R-variant, *Mab* subsp. *abscessus* CIP104536^T S-variant, *Mab* subsp. *bolletii*, and *Mab* subsp. *massiliense* were grown to mid-log phase in Middlebrook 7H9 broth medium supplemented with 0.5% glycerol, 0.05% Tween 80, and 10% ADS supplement. The growth inhibition dose-response assay was performed according to the method previously described[14]. Briefly, 198 µL of the mycobacterial cultures with the OD_{600} adjusted to 0.005 was dispensed into each well on the 96-well flat bottom plate containing 2 µL of the drug compound. The assay plates were incubated at 32 °C for 2 days. After the incubation, the cultures in all plates were all manually resuspended and the OD_{600} was measured using Synergy H1 multiplate reader (BioTek), and analysis was performed using GraphPad Prism 7.04 software[33].

Intracellular ATP quantification

Intracellular ATP levels were determined with BacTiter-Glo™ Microbial Cell Viability Assay (Promega)[42]. 198 µL of the mycobacterial cultures with the OD_{600} adjusted to 0.05 was dispensed into each well on the 96-well flat bottom plate containing 2 µL of the drug compound. The assay plates were incubated at 32 °C for 1 day and measurement was performed by mixing 50 µL of the mycobacterial culture with equal amount of BacTiter-Glo™ reagent. Emitted luminescence was measured using Synergy H1 multiplate reader (BioTek) and data analysis was performed using GraphPad Prism 7.04 software[33].

Methylene Blue Assay

Oxygen consumption in whole bacteria was measured using methylene blue as a detector. Mycobacterial cultures OD_{600} were adjusted to 0.4 and 1.6 mL of each culture was dispensed into a two-millilitre screw-cap glass vial. 3.2 µL of 0.5% methylene blue was added into each vial for a final concentration of 0.001%. Vials were tightly sealed and incubated at 32 °C in an anaerobic chamber. The vials were removed from the incubator on the second and third days for image recording.

Oxygen consumption assays using the Seahorse XFe96 analyzer

Measurement was performed using the Seahorse XFe96 analyzer (Agilent Technologies, USA). In this assay, Laminin/Poly-D-lysine was used as cell adhesive to attach the cells onto the plate. Laminin/Poly-D-lysine was washed with sterile water after dispensing onto the bottom of the assay plate. *Mab* cultures: CIP104536^T wild-type, D311E/L314A, D311E/L314I, F158Y/D311E/L314A and G179S/D311E/L314A/C393A) were grown in 7H9-ADS-glycerol medium until it reaches log phase (OD_{600}: 0.4 to 0.6). Subsequently, the cells were washed twice in 10% 7H9-ADS medium in phosphate-buffered saline (PBS) and adjusted to an OD_{600} of 0.2. 50 µL of the washed cultures were dispensed into each of the coated wells of the assay plate and centrifuged at 3,800 rpm for 10 minutes. After which, 130 µL 10 % 7H9-ADS medium in PBS was dispensed into each well. Q203 was diluted to concentrations of 1 µM and 50 µM in 10 % 7H9-ADS medium in PBS and loaded into the drug port. Measurement was taken every cycle consisting of four minutes of continuous reading followed by three minutes of continuous mixing. The basal oxygen consumption rate was determined using three readings before the introduction of Q203. Data was collected using Wave 2.6.0.31 software and analyzed using GraphPad Prism 7.04 software[33].

Bacteria Viability Experiment

Mab CIP104536^T strain was grown in 7H9-ADS-glycerol medium until it reached log phase (OD_{600}: 0.4 to 0.6). The cells were washed twice in 7H9-ADS medium and adjusted to an OD_{600} of 0.005. Test compounds and vehicular control were dispensed into 24-well plates, respectively,

containing the adjusted *Mab* cultures. Dilutions of the respective conditions were plated on Luria-Bertani (LB) plates and incubated at 32 °C. Bacterial viability was determined by enumerating colony-forming units (CFU) after plating on agar plates. The number of colonies was counted after agar plates were incubated at 32 °C for 3–4 days.

Checkerboard assay

Twofold serial dilutions were performed to allow for 11 different concentrations of ND-011458 (20 µM to 0.1 µM) to be tested for interaction with seven different concentrations of CFZ (2.4 µM to 0.03 µM). Each 96-well plate had a drug-free bacterial culture control well. *Mab* was cultured in 7H9-ADS-glycerol medium and grown to mid-exponential phase. Subsequently, the culture was washed and diluted to an OD_{600} of 0.005 in 7H9-ADS medium. 200 µL of the adjusted culture was dispensed into each well and incubated for 3 days at 32 °C. The OD_{600} of the cultures was measured using a Synergy H1 multiplate reader (BioTek), and analysis was performed using GraphPad Prism 7.04 software[33].

The calculation of the fractional inhibitory concentration index (FICI) was done to analyze the results. The FICI is calculated as (MIC of drug A in combination / MIC of drug A alone) + (MIC of DARQ B in combination / MIC of DARQ B alone). This calculation was done only for wells that showed 50% inhibition of bacterial culture growth compared to drug-free bacterial culture wells. A FICI of ≤ 0.5 indicates synergy, a FICI of > 0.5 to 4 indicates additivity (no interaction), and a FICI of > 4 indicates antagonism[43].

Statistics & Reproducibility

No statistical method was used to predetermine sample size. Data was only excluded in the case of the cryo-EM experiment where particles with lesser quality were excluded by iterative 2D and 3D classifications as generally endorsed by cryo-EM studies. Randomization was performed only in the cryo-EM study at the 3D reconstruction stage, as generally demanded by cryo-EM studies, for the calculation of FSC curves illustrated in the Supplementary Figs.; The investigators were not blinded to allocation during experiments and outcome assessment.

Reporting summary

Further information on research design is available in the Nature Portfolio Reporting Summary linked to this article.

Data availability

All relevant data are contained within the article. Structural data that supports the findings of this study are openly available from the Protein Data Bank (https://www.rcsb.org; PDB ID 9WCX, 9WCY) and the EM Data Bank (https://www.ebi.ac.uk/emdb/; EMDB ID EMD-65878, EMD-65879). Source data are provided with this paper.

References

1. Liang, Y. & Rubinstein, J. L. Structural analysis of mycobacterial electron transport chain complexes by cryoEM. *Biochemical Soc. Trans.* **51**, 183–193 (2023).
2. Bald, D., Villellas, C., Lu, P. & Koul, A. Targeting Energy Metabolism in *Mycobacterium tuberculosis*, a New Paradigm in Anti-mycobacterial Drug Discovery. *mBio* **8**, https://doi.org/10.1128/mbio.00272-00217, (2017).
3. Gong, H. et al. An electron transfer path connects subunits of a mycobacterial respiratory supercomplex. *Science* **362**, eaat8923 (2018).
4. Wiseman, B. et al. Structure of a functional obligate complex III_2IV_2 respiratory supercomplex from *Mycobacterium smegmatis*. *Nat. Struct. Mol. Biol.* **25**, 1128–1136 (2018).
5. Mathiyazakan, V., Wong, C.-F., Harikishore, A., Pethe, K. & Grüber, G. Cryo-Electron Microscopy Structure of the Mycobacterium tuberculosis Cytochrome *bcc*:aa_3 Supercomplex and a Novel Inhibitor Targeting Subunit Cytochrome cI. *Antimicrobial Agents Chemother.* **67**, e01531–01522 (2023).
6. Pethe, K. et al. Discovery of Q203, a potent clinical candidate for the treatment of tuberculosis. *Nat. Med.* **19**, 1157–1160 (2013).
7. Jager, V. R. D. et al. Telacebec (Q203), a New Antituberculosis Agent. *N. Engl. J. Med.* **382**, 1280–1281 (2020).
8. Scherr, N. et al. Targeting the Mycobacterium ulcerans cytochrome bc_1:aa_3 for the treatment of Buruli ulcer. *Nat. Commun.* **9**, 5370 (2018).
9. Lahiri, R., Adams, L. B., Thomas, S. S. & Pethe, K. Sensitivity of *Mycobacterium leprae* to Telacebec. *Emerg. Infect. Dis.* **28**, 749–751 (2022).
10. Chauhan, P. et al. Response of *Mycobacterium smegmatis* to the Cytochrome *bcc* Inhibitor Q203. *Int. J. Mol. Sci.* **23**, https://doi.org/10.3390/ijms231810331 (2022).
11. Johansen, M. D., Herrmann, J. L. & Kremer, L. Non-tuberculous mycobacteria and the rise of *Mycobacterium abscessus*. *Nat. Rev. Microbiol* **18**, 392–407 (2020).
12. Dartois, V. & Dick, T. Therapeutic developments for tuberculosis and nontuberculous mycobacterial lung disease. *Nat. Rev. Drug Discov.* **23**, 381–403 (2024).
13. Luthra, S., Rominski, A. & Sander, P. The Role of Antibiotic-Target-Modifying and Antibiotic-Modifying Enzymes in *Mycobacterium abscessus* Drug Resistance. *Front Microbiol* **9**, 2179 (2018).
14. Sorayah, R. et al. Naturally-Occurring Polymorphisms in QcrB Are Responsible for Resistance to Telacebec in *Mycobacterium abscessus*. *ACS Infect. Dis.* **5**, 2055–2060 (2019).
15. Zhou, S. et al. Structure of *Mycobacterium tuberculosis* cytochrome *bcc* in complex with Q203 and TB47, two anti-TB drug candidates. *Elife* **10**, https://doi.org/10.7554/eLife.69418 (2021).
16. Lechartier, B. & Cole, S. T. Mode of Action of Clofazimine and Combination Therapy with Benzothiazinones against *Mycobacterium tuberculosis*. *Antimicrob. Agents Chemother.* **59**, 4457–4463 (2015).
17. Murphy, K. C. et al. ORBIT: a New Paradigm for Genetic Engineering of Mycobacterial Chromosomes. *mBio* **9**, https://doi.org/10.1128/mBio.01467-18 (2018).
18. Meng, E. C. et al. UCSF ChimeraX: Tools for structure building and analysis. *Protein Sci.* **32**, e4792 (2023).
19. Page, C. C., Moser, C. C., Chen, X. & Dutton, P. L. Natural engineering principles of electron tunnelling in biological oxidation–reduction. *Nature* **402**, 47–52 (1999).
20. Yanofsky, D. J. et al. Structure of mycobacterial CIII(2)CIV(2) respiratory supercomplex bound to the tuberculosis drug candidate telacebec (Q203). *Elife* **10**, https://doi.org/10.7554/eLife.71959 (2021).
21. Kao, W. C. et al. Structural basis for safe and efficient energy conversion in a respiratory supercomplex. *Nat. Commun.* **13**, 545 (2022).
22. Agmon, N. The Grotthuss mechanism. *Chem. Phys. Lett.* **244**, 456–462 (1995).
23. Zhu, G. et al. The Unusual Homodimer of a Heme-Copper Terminal Oxidase Allows Itself to Utilize Two Electron Donors. *Angew. Chem. Int Ed. Engl.* **60**, 13323–13330 (2021).
24. Lamprecht, D. A. et al. Turning the respiratory flexibility of Mycobacterium tuberculosis against itself. *Nat. Commun.* **7**, 12393 (2016).
25. Sarewicz, M. & Osyczka, A. Electronic connection between the quinone and cytochrome C redox pools and its role in regulation of mitochondrial electron transport and redox signaling. *Physiol. Rev.* **95**, 219–243 (2015).
26. Shen, G. H. et al. High efficacy of clofazimine and its synergistic effect with amikacin against rapidly growing mycobacteria. *Int J. Antimicrob. Agents* **35**, 400–404 (2010).

27. Dupont, C. et al. Bedaquiline Inhibits the ATP Synthase in Mycobacterium abscessus and Is Effective in Infected Zebrafish. *Antimicrob. Agents Chemother.* **61**, https://doi.org/10.1128/aac.01225-01217, (2017).
28. Sarathy, J. P. et al. TBAJ-876, a 3,5-Dialkoxypyridine Analogue of Bedaquiline, Is Active against Mycobacterium abscessus. *Antimicrob. Agents Chemother.* **64**, https://doi.org/10.1128/aac.02404-19 (2020).
29. Ragunathan, P. et al. High efficacy of the F-ATP synthase inhibitor TBAJ-5307 against nontuberculous mycobacteria *in vitro* and *in vivo*. *J. Biological Chem.* **300**, https://doi.org/10.1016/j.jbc.2023.105618 (2024).
30. Ragunathan, P., Dick, T. & Grüber, G. Anti-*Mycobacterium abscessus* Activity of Tuberculosis F-ATP Synthase Inhibitor GaMF1. *Antimicrob. Agents Chemother.* **66**, e0001822 (2022).
31. Ragunathan, P. et al. SQ31f is a potent non-tuberculous mycobacteria antibiotic by specifically targeting the mycobacterial F-ATP synthase. *J. Antimicrobial Chemother.* **80**, 270–280 (2024).
32. Sorayah, R., Moraski, G. C., Barkan, D. & Pethe, K. The QcrB Inhibitors TB47 and Telacebec Do Not Potentiate the Activity of Clofazimine in *Mycobacterium abscessus*. *Antimicrob. Agents Chemother.* **65**, e0096421 (2021).
33. Motulsky, H. *Analyzing Data with GraphPad Prism*. (GraphPad Software Incorporated, 1999).
34. Zheng, S. Q. et al. MotionCor2: anisotropic correction of beam-induced motion for improved cryo-electron microscopy. *Nat. Methods* **14**, 331–332 (2017).
35. Rohou, A. & Grigorieff, N. CTFFIND4: Fast and accurate defocus estimation from electron micrographs. *J. Struct. Biol.* **192**, 216–221 (2015).
36. Punjani, A., Rubinstein, J. L., Fleet, D. J. & Brubaker, M. A. cryoSPARC: algorithms for rapid unsupervised cryo-EM structure determination. *Nat. Methods* **14**, 290–296 (2017).
37. Punjani, A., Zhang, H. & Fleet, D. J. Non-uniform refinement: adaptive regularization improves single-particle cryo-EM reconstruction. *Nat. Methods* **17**, 1214–1221 (2020).
38. Noble, M. & Perrakis, A. Model building and refinement. *Acta Crystallographica Section D* **60**, https://doi.org/10.1107/S0907444904028586 (2004).
39. Liebschner, D. et al. Macromolecular structure determination using X-rays, neutrons and electrons: recent developments in Phenix. *Acta Crystallogr D. Struct. Biol.* **75**, 861–877 (2019).
40. Waterhouse, A. et al. SWISS-MODEL: homology modelling of protein structures and complexes. *Nucleic Acids Res.* **46**, W296–W303 (2018).
41. Davis, I. W. et al. MolProbity: all-atom contacts and structure validation for proteins and nucleic acids. *Nucleic Acids Res.* **35**, W375–W383 (2007).
42. Rao, S. P., Alonso, S., Rand, L., Dick, T. & Pethe, K. The protonmotive force is required for maintaining ATP homeostasis and viability of hypoxic, nonreplicating *Mycobacterium tuberculosis*. *Proc. Natl. Acad. Sci. USA.* **105**, 11945–11950 (2008).
43. Odds, F. C. Synergy, antagonism, and what the chequerboard puts between them. *J. Antimicrob. Chemother.* **52**, 1 (2003).

Acknowledgements

The authors acknowledge the Cryo-Electron Microscopy Facility at the Center for Bioimaging Science, Department of Biological Science, National University of Singapore for technical assistance in data collection of the apo enzyme complex. We also acknowledge the NTU Institute of Structural Biology, Nanyang Technological University, Singapore for the usage of the Cryo-Electron Microscopy Facility for the compound-bound enzyme complex. This work was supported by the National Research Foundation (NRF) Singapore, NRF Competitive Research Programme (CRP), Grant Award Number NRF-CRP27-2021-0002. E.T.X.Y. was funded by an NTU Research Scholarship. G.M. was supported by grant R37AI054193 by the National Institute of Health (NIH), United States. Funding for the Montana State Mass Spectrometry Facility (RRID: SCR_012482) used in this publication was made possible in part by the MJ Murdock Charitable Trust, the National Institute of General Medical Sciences of the National Institutes of Health under Award Numbers P20GM103474 and S10OD28650, and the MSU Office of Research and Economic Development. NMR spectra were recorded at Montana State University on a 400 MHz NMR spectrometer housed in MSU's NMR Center (RRID:SCR_026334). Financial support for the NMR instruments and operations have been provided in part by the NIH SIG program (1S10RR13878 and 1S10RR026659), the National Science Foundation (NSF-MRI:DBI-1532078; NSF-MRI:CHE-2018388), the Murdock Charitable Trust Foundation (2015066:MNL), and MSU's Office of Research & Economic Development, and Graduate Education at MSU.

Author contributions

V.M., E.T.X.Y., G.M. and G.G. designed the experiments; V.M., E.T.X.Y., G.M., S.B. and G.G. formal analysis; V.M., E.T.X.Y., G.M., S.B., W.-G.S. investigation; V.M. and G.G. writing-original draft; all authors; Writing - Review and Editing; G.M., K.P. and G.G. funding acquisition.

Competing interests

G.G, V.M., G.M, and P.K. are inventors on the patent 63/773,541, which is related to the inhibitor described in this article. The remaining authors declare no competing interests.

Additional information

Supplementary information The online version contains supplementary material available at https://doi.org/10.1038/s41467-026-70805-5.

Correspondence and requests for materials should be addressed to Gerhard Grüber.

Peer review information *Nature Communications* thanks Vinothkumar Kutti Ragunath, and the other, Edward Berry, anonymous, reviewer(s) for their contribution to the peer review of this work. A peer review file is available.